Precursory Signals to Injection Induced Fault Reactivation in the Laboratory Using Active Ultrasonic Monitoring Methods

Veltmeijer, A.; Naderloo, M.; Pluymakers, A.; Barnhoorn, A.

DOI
10.1029/2023JB028505

Publication date
2024

Document Version
Final published version

Published in
Journal of Geophysical Research: Solid Earth

Citation (APA)
Veltmeijer, A., Naderloo, M., Pluymakers, A., & Barnhoorn, A. (2024). Precursory Signals to Injection Induced Fault Reactivation in the Laboratory Using Active Ultrasonic Monitoring Methods. *Journal of Geophysical Research: Solid Earth*, *129*(2), Article e2023JB028505. https://doi.org/10.1029/2023JB028505

JGR Solid Earth

RESEARCH ARTICLE
10.1029/2023JB028505

Precursory Signals to Injection Induced Fault Reactivation in the Laboratory Using Active Ultrasonic Monitoring Methods

A. Veltmeijer[1], M. Naderloo[1], A. Pluymakers[1], and A. Barnhoorn[1]

[1]Faculty of Civil Engineering and Geosciences, Section of Applied Geophysics and Petrophysics, Delft University of Technology, Delft, The Netherlands

Key Points:

- Time-lapse monitoring of coda waves can be used to monitor injection-induced fault reactivation in the laboratory
- Different stages of fault reactivation in the laboratory seismic cycle can be identified using ultrasonic monitoring
- Transmission measurements change prior to injection-induced fault reactivation on smooth and rough fault planes

Correspondence to:
A. Veltmeijer,
a.v.veltmeijer@tudelft.nl

Citation:
Veltmeijer, A., Naderloo, M., Pluymakers, A., & Barnhoorn, A. (2024). Precursory signals to injection induced fault reactivation in the laboratory using active ultrasonic monitoring methods. *Journal of Geophysical Research: Solid Earth*, *129*, e2023JB028505. https://doi.org/10.1029/2023JB028505

Received 8 DEC 2023
Accepted 24 JAN 2024

Author Contributions:
Conceptualization: A. Veltmeijer, M. Naderloo, A. Pluymakers, A. Barnhoorn
Data curation: A. Veltmeijer
Formal analysis: A. Veltmeijer
Funding acquisition: A. Barnhoorn
Investigation: A. Veltmeijer, M. Naderloo
Methodology: A. Veltmeijer, M. Naderloo
Project administration: A. Barnhoorn
Supervision: A. Barnhoorn
Validation: A. Veltmeijer
Writing – original draft: A. Veltmeijer
Writing – review & editing: A. Pluymakers, A. Barnhoorn

Abstract Induced earthquakes are still highly unpredictable, and often caused by variations in pore fluid pressure. Monitoring and understanding the mechanisms of fluid-induced fault slip is essential for seismic risk mitigation and seismicity forecasting. Fluid-induced slip experiments were performed on critically stressed faulted sandstone samples, and the evolution of the actively sent ultrasonic waves throughout the experiment was measured. Two different fault types were used: smooth saw-cut fault samples at a 35° angle, and a rough fault created by in situ faulting of the samples. Variations in the seismic slip velocity and friction along the fault plane were identified by the coda of the ultrasonic waves. Additionally, ultrasonic amplitudes show precursory signals to laboratory fault reactivation. Our results show that small and local variations in stress before fault failure can be inferred using coda wave interferometry for time-lapse monitoring, as coda waves are more sensitive to small perturbations in a medium than direct waves. Hence, these signals can be used as precursors to laboratory fault slip and to give insight into reactivation mechanisms. Our results show that time-lapse monitoring of coda waves can be used to monitor local stress changes associated with fault reactivation in this laboratory setting of fluid-induced fault reactivation. This is a critical first step toward a method for continuous monitoring of natural fault zones, contributing to seismic risk mitigation of induced and natural earthquakes.

Plain Language Summary Activities underground, such as gas extraction or fluid injection, can disturb the natural stresses present and cause human-induced earthquakes along pre-existing faults. Even though they are related to engineering, these earthquakes are currently unpredictable. Monitoring and understanding how these earthquakes occur are essential to progress with mitigation measures and earthquake forecasting. Here, we inject fluid to reactivate faulted sandstone samples in the laboratory, while monitoring what happens with ultrasonic waves that are being sent continuously through the faulted sample as we attempt to create a laboratory earthquake. We show that by detecting small changes in these ultrasonic waves we can identify the stages of fault movement, including precursors, in these simplified laboratory fault zones. This implies that similar signals could potentially be used as precursors to fault movement in other settings as well, which is a critical first step toward a method for monitoring of the subsurface in real life, contributing toward a method of seismic risk mitigation of induced and natural earthquakes.

1. Introduction

Forecasting earthquakes has received much interest for many years. Increasing human activities in the subsurface have caused substantial earthquakes in more densely populated areas (e.g., M3.4 Basel (2006), Switzerland, M3.6 Groningen, the Netherlands (2012), and M5.4 Pohang, South Korea (2017)), with serious consequences for subsurface use, halting a geothermal project in Basel, and onshore gas production in Groningen. Thus, effective subsurface monitoring and seismic forecasting are essential to limit the risk and mitigate seismic hazards. In general, the common mechanisms occurring during the seismic cycle are well known (Figure 1) (Shreedharan et al., 2021a). This involves initial stress build-up during the inter-seismic phase, during which the fault experiences creep, and fault healing. In the pre-seismic phase the first slip instabilities nucleate where the local stress exceeds the fault strength. This accelerates creep until a seismic event is generated in the co-seismic reactivation phase, during which a large slip event takes place rapidly and stress on the fault is released. In the post-seismic phase, the system will experience creep and renewed fault healing. Currently, natural earthquake forecasts are made using reoccurrence intervals of the seismic cycle, that is, the average duration of the post-seismic phase (Shimazaki & Nakata, 1980), or using the precursor events during the pre-seismic phase, such as the average

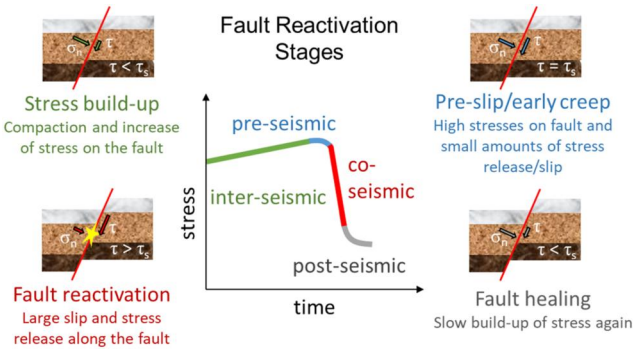

Figure 1. Cartoon of fault movement and the corresponding laboratory seismic/fault reactivation stages. Fault instability and movement occur when the shear stress τ is larger than the shear strength τ_s.

earthquake size distribution (*b*-value) (Gulia et al., 2020). For induced seismicity, forecasting can be done using probabilistic models (Király-Proag et al., 2016; Langenbruch et al., 2018), which can include various production scenarios (Dempsey & Suckale, 2017). In laboratory settings, frictional sliding experimental studies have been performed using passive acoustic monitoring (Cartwright-Taylor et al., 2022; Guglielmi et al., 2015; Noël et al., 2019; Ye & Ghassemi, 2020), mostly to investigate fault mechanics and often to target the onset of the first small and precursory slip events of the pre-seismic phase. However, robust, and reliable predicting of fault failure and the resulting earthquake has proven to be a challenging task (Geller, 1997; Hough, 2009; Kagan & Jackson, 1991; Pritchard et al., 2020), even for experimental faults under controlled laboratory settings (Main & Meredith, 1989).

Pore fluid pressure changes play an important role in the frictional strength and stability of faults and are considered the main trigger for induced seismicity in several real world applications such as hydrocarbon extraction or geothermal energy production (Guglielmi et al., 2015; Kaproth & Marone, 2013a; Stanchits et al., 2011; L. Wang et al., 2020). In contrast to the natural seismic cycle, in these cases instabilities are created locally due to the local pore pressure variations. These cause perturbations in stress magnitude along the fault. Consequently, the pre-seismic phase can arise when the shear strength of the fault plane is exceeded, which then ultimately results in fast shear slip along pre-existing faults and fractures (L. Wang et al., 2020), that is, the seismic phase in Figure 1. To date, few studies focus on predicting fluid-induced seismicity specifically, and hence, predicting the extent of these pore pressure-induced stress changes, and therefore the potential onset and exact location of failure and seismicity remains very challenging.

Generally speaking, stress changes can be inferred by analyzing the change in acoustic or seismic velocity (Cartwright-Taylor et al., 2022; Xie et al., 2018). For intact rocks, it has been shown that seismic velocities change in response to stress, for example, due to compression of the rocks (Barnhoorn et al., 2018; Winkler & Nur, 1979). In particular, it has been shown that the coda of the acoustic wave traveling through the medium is exceptionally sensitive to changes in the microstructure (Snieder et al., 2002; Stähler et al., 2011; Zhang et al., 2012; Zotz-Wilson et al., 2019), where the use of coda wave interferometry can predict the onset of failure before the stress drops in intact rock loaded under a constant rate. However, only a very limited number of laboratory fault sliding studies included continuous active ultrasonic monitoring (Kaproth & Marone, 2013a; Passelègue et al., 2018; Shreedharan et al., 2019, 2020, 2021a; Veltmeijer et al., 2023a). Moreover, these studies focused only on the elastic wave velocity and changes in amplitude for sliding on smooth faults. Results show precursory changes in elastic wave velocity (Kaproth & Marone, 2013b; Passelègue et al., 2018; Veltmeijer et al., 2023a) and amplitude (Shreedharan et al., 2019, 2020, 2021a; Veltmeijer et al., 2022) during the pre-seismic phase of fault reactivation (Figure 1). However, the relations between these changes in the elastic wave properties and the mechanisms of precursors to failure remain poorly understood. Moreover, it is unknown if monitoring techniques based on arrival time and amplitude would still work for complex, rough fault surfaces, which can be considered more representative of natural fault zones (Frank et al., 2020). Given the success of coda wave interferometry on detecting oncoming failure in intact rocks, we also test the possibilities of coda wave interferometry for monitoring the laboratory seismic cycle with different fluid injection protocols in smooth and rough faults.

This paper aims to monitor slip by identifying precursors from the temporal evolution of ultrasonic seismic waves and to understand the connection between precursors and mechanisms of failure. We present the results of injection-driven reactivation of fault experiments in combination with continuous active ultrasonic monitoring. Fluid pressure was increased cyclically and stepwise to induce slip on the critically stressed saw-cut and in situ faulted permeable Red-Felser sandstones.

2. Materials and Methods

2.1. Rock Samples

Red Felser sandstones were used in the experiments. These sandstones originate from the Rotliegend formation, which is the same formation as the Groningen reservoir sandstones, and are obtained from a quarry near

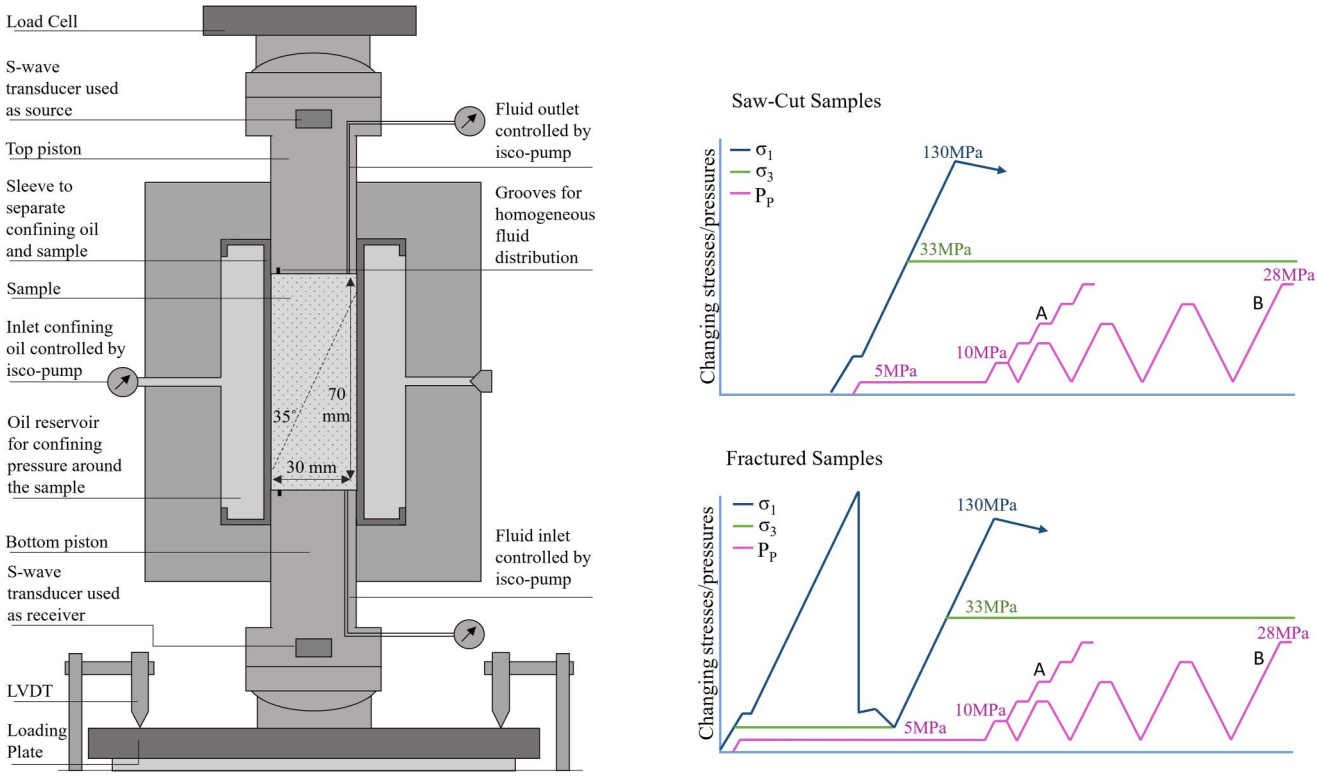

Figure 2. Left: Scheme of Hoek-cell used for triaxial experiments (not to scale). Right: Scheme of loading and injection protocol for the saw-cut (top) and fractured (bottom) samples. In both cases, protocol A shows stepwise injection and protocol B cyclic injection. The loading plate is fixed during injection, hence the axial stress is allowed to drop during fault reactivation due to fluid injection.

Kaiserslautern, in Germany (Naderloo et al., 2023; van Uijlen, 2013). The rock properties, specifically lithology, porosity, and permeability, of the Red Felser are very similar to the Slochteren sandstone (Eradus, 2019). The intact rock samples have a porosity of 21.4% ± 0.7% and were 30 ± 0.1 mm in diameter and 70 ± 0.1 mm in length.

2.2. Experimental Protocol

The experiments were conducted using a Hoek-cell, a triaxial apparatus (Figure 2) which is placed in an in-house built uniaxial loading frame with a 500 kN loadcell. Confining pressure and pore fluid pressure were maintained using an ISCO pump model 100DM. Fluid pressure was imposed at the bottom of the sample but was measured at the top and bottom of the sample. The difference in fluid pressure between top and bottom was within ±0.2 MPa. We recorded the shortening of the sample using two Solartron AX/1/S linear variable displacement transducers (LVDTs) with a ±0.1 μm precision. All displacement data was corrected for elastic machine and piston deformation afterward.

Four types of experiments were performed using two fluid injection protocols, namely stepwise and cyclic fluid injection, on smooth and rough faulted samples. By performing multiple repeat tests for the different configurations, the consistency of the acoustic responses has been confirmed. The first sample type has a smooth saw-cut fault, cut at an angle of 35° to the vertical axis (i.e., similar to Ye and Ghassemi (2020)). The tips of the saw-cut plane were slightly rounded to prevent breaking of the edges, resulting in an approximately elliptical fault surface of 45 ± 0.7 mm in length and 29.6 ± 0.1 mm in width (Figure 3a). The second sample type has a rough fault created in situ in the laboratory assembly, which is assumed to be more representative of natural rough faults. Prior to testing, all samples were vacuum-saturated with tap water. For the sample with a rough fault, prior to injection, we fractured an intact sample at 10 MPa confining and 5 MPa fluid pressure. After the fracture was formed, loading of the sample was continued in displacement control for 2 min to eliminate cohesive strength and to slightly open the fracture, to promote slip along the created fracture during the injection stage of the

Figure 3. Pictures of (dried) samples before (a) and after the experiment was finished (b and c). Note that the tips of the saw-cut are ground off <3 mm, but the overall shape is still elliptical, with dimensions [45 ± 0.7 mm/29.6 ± 0.1 mm]. The middle (b) shows a sample after stepwise injection and the right (c) after cyclic injection. The formed gouge is visible as the patchy whitish powder on the saw-cut fault surface. The patterns of final gouge distribution were different after each experiment, without any relationship to experimental parameters.

experiment. After creating the rough fault, the experiment proceeded with the same loading and injection protocol as the saw-cut fault samples (Figure 2).

Before the fluid injection protocols starts, all faulted samples were stressed to a confining pressure of 33 and 5 MPa fluid pressure. Note that the confining pressure ($\sigma 3 = \sigma 2$) was held constant during the entire experiment. Then the sample was loaded with a constant vertical strain rate of $0.0005 s^{-1}$ until the stress-strain curve starts to deviate from linearity (the start of fault reactivation), and reaching a critical stressed condition of the shear stress (τ) (L. Wang et al., 2020; Ye & Ghassemi, 2020)). Here the position of the axial loading press was fixed and held constant. After 10 min waiting time, to allow the settling of the sample and assembly, the fluid injection started.

In the first protocol, the stepwise injection (A in Figure 2), the fluid pressure was increased stepwise by 5 MPa at a rate of 2 MPa/min with 5 min of waiting time in between each step until the maximum pressure of 28 MPa was reached. In the second protocol, the cyclic injection (B in Figure 2), the fluid pressure was returned to the initial pressure of 5 MPa after each increasing step (5 MPa above the previous pressure) of the fluid pressure, and using the same rate of 2 MPa/min but with 3 min waiting time in between each cycle. The fluid pressure was cyclically increased to the same maximum of 28 MPa.

After finishing the experiment, the sample with the created rough fault was removed from the Hoek-cell and scanned in a Nanotom NF180 microCT scanner with a resolution of (voxel size) 64 µm and processed using Avizo © software.

Active ultrasonic seismic monitoring was performed on all experiments, simultaneously with the mechanical data acquisition. The waveforms were generated by an Agilent 33210A waveform generator, amplified by an RF Power amplifier, sent and received using Olympus 1 MHz/.5" v153 transducers, and finally recorded using a Yokogawa DL9240L oscilloscope. The transducers are integrated into the pistons of the loading system. Two S-wave transducers were used, with the source at the top and the receiver at the bottom of the samples. The transducers were placed such that the polarization of the shear source and receiver was aligned. The peak operating frequency of the S-wave transducers is 1 MHz and the ultrasonic signals were recorded every 3 s for 100 µs. To increase the signal-to-noise ratio, every recorded waveform is a stack of 256 S-waves, each sent 4 ms apart (Figure 4a).

2.3. Data Analysis

During the experiment, signals were logged for force (N), confining pressure (bar), displacement (µ m), pore fluid pressure (bar), wave arrival time (s), and amplitude (volt). The shear stress (τ), friction coefficient (μ), and effective normal stress (σ_n) along the fault plane are determined using the principal stresses, $\sigma 1$ and $\sigma 2 = \sigma 3$, derived from the force and confining pressure data respectively, and the fluid pressure (P_f) as given by

$$\mu = \frac{\tau}{\sigma_n - P_f}, \quad (1)$$

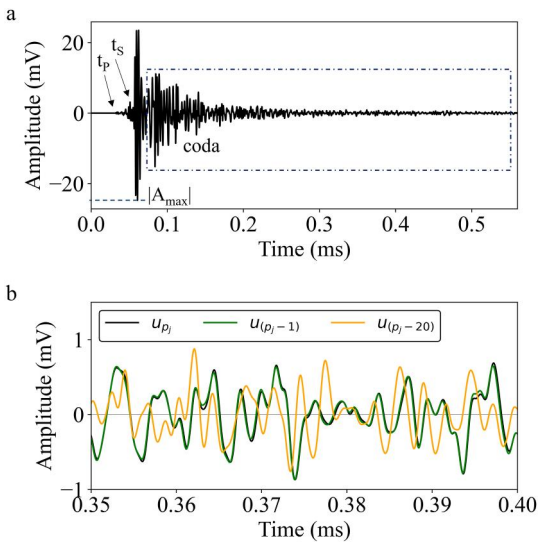

Figure 4. Example of a recorded waveform (a) showing the arrival time of the P-wave (t_P) and of the S-wave (t_S) as well as the maximum transmitted amplitude of the S-waves. The length of the coda is indicated by the box and starts at $t = 1.5t_S$. Part of the coda is enlarged in (b) to illustrate the shift in the coda over time, showing the to-be-correlated wavefield $u_{p_j}(t)$ and the reference wavefield $u_{p_j-N}(t)$ with $N = 1$ and 20.

with

$$\tau = \frac{\sigma_1 - \sigma_3}{2}\sin(2\alpha), \tag{2}$$

and

$$\sigma_n = \frac{\sigma_1 + \sigma_3 - 2P_f}{2} - \frac{\sigma_1 - \sigma_3}{2}\cos(2\alpha), \tag{3}$$

where σ_1 and σ_3 are the axial and radial stress respectively and α is the fault angle with respect to the vertical (Byerlee, 1967; L. Wang et al., 2020). The τ and σ_n are corrected for a changing contact area of the fault due to fault slip. The fault slip (s) is determined from the total axial displacement (Δl_{LVDT}), corrected for the displacement of the loading machine (Δl_{MD}) and the rock matrix (Δl_{RM}) (L. Wang et al., 2020), as follows:

$$s = \frac{\Delta l_{\mathrm{LVDT}} - \Delta l_{\mathrm{MD}} - \Delta l_{\mathrm{RM}}}{\cos(\alpha)}. \tag{4}$$

The displacement of the loading machine (Δl_{MD}) and the rock matrix (Δl_{RM}) can be estimated using the stiffness of the machine (K_M) and rock matrix (K_{rock}), and the force drop (F_N), rewriting Equation 4 into:

$$s = \frac{\Delta l_{\mathrm{LVDT}} - \frac{F_N}{K_M} - \frac{F_N}{K_{\mathrm{rock}}}}{\cos(\alpha)}. \tag{5}$$

For the stiffness of the machine and that of the rock matrix we performed a series of calibration experiments using aluminum reference samples and intact rock samples. The recorded waveforms are analyzed using the maximum transmitted amplitude of the recorded P- or S-wave as transmissivity $T = |A_{\mathrm{max}}|$ (Shreedharan et al., 2020). In addition to the arriving amplitudes, coda wave interferometry (CWI) is used to monitor the velocity change between two recorded waves. The theory of CWI as presented by Snieder (2002) states that the unperturbed wavefield $u_u(t)$ can be written as a sum of all possible paths (p) the waves can travel through the medium, where t is time and $A_p(t)$ is the wave along travel path P:

$$u_u(t) = \sum_P A_p(t). \tag{6}$$

Each scatterer in the medium is assumed to have stationary properties. Therefore, the scatterer does not change its size, shape, density, and velocity. Additionally, the distance between the individual scatterers is assumed to be much larger than the dominant wavelength ($l \gg \lambda$). The major difference between the wavefields, when the medium changes over time, is the arrival times of the waves propagating along each travel path p. The perturbed wavefield can thus be represented as

$$u_p(t) = \sum_P A_p(t - \delta t_p), \tag{7}$$

where δt_p is the travel time change along the path P. This implies that the perturbed wavefield shows only a change in time and does not change the dispersion of the wavefield. By comparing the wave fields the variations in the medium can be assessed. The cross-correlation coefficient is a common method to quantify these variations. The cross-correlation coefficient (CC) for a time window of width $2t_w$ and centered around time t_k is given by

$$\mathrm{CC}(t_s) = \frac{\int_{t_k - t_w}^{t_k + t_w} u_u(t)\, u_p(t + t_s)\, dt}{\sqrt{\int_{t_k - t_w}^{t_k + t_w} u_u^2(t)\, dt \int_{t_k - t_w}^{t_k + t_w} u_p^2(t)\, dt}}. \tag{8}$$

The cross-correlation coefficient (CC) reaches its maximum if the travel time perturbation δt across all possible perturbed paths P is

$$\delta t = t_s. \tag{9}$$

The velocity change can be written as the average slope of δt versus t, assuming the time shift is constant in the considered time window, as follows:

$$\frac{\delta v}{v} = \frac{\delta t}{t} \tag{10}$$

To investigate the changes in material scattering, the decorrelation coefficient (K) is determined. The method of coda wave decorrelation (CWD) introduced by Larose et al. (2010) is based on the theory of Snieder (2006). The decorrelation coefficient is formulated as

$$K(t_s) = 1 - \mathrm{CC}(t_s) = 1 - \frac{\int_{t_k-t_w}^{t_k+t_w} u_{p_j-N}(t)\, u_{p_j}(t+t_s)\, dt}{\sqrt{\int_{t_k-t_w}^{t_k+t_w} u_{p_j-N}^2(t)\, dt \int_{t_k-t_w}^{t_k+t_w} u_{p_j}^2(t)\, dt}}, \tag{11}$$

where N is the number of measurements the reference wavefield $u_{p_j-N}(t)$ is lagging behind the to-be-correlated wavefield $u_{p_j}(t)$ (Figure 4b). For continuously monitoring the evolving scattering medium, a moving reference wavefield is used (cf. Grêt et al., 2006; Zotz-Wilson et al., 2019). The decorrelation coefficient K is related to the changes in material scattering due to the addition or removal of scatter(ers) in the medium (Planès et al., 2014, 2015). The coda waves seem random due to the complex paths they take through the medium, but the changes they are subjected to are strongly related to the position and strength of the changes in the medium (Planès et al., 2014). The scattering in a medium along the transport mean free path l can be described using the cross-sectional area of a single scatterer σ and the density of scatterers ρ (Planès et al., 2014). The total scattering coefficient, as described by Aki and Chouet (1975), is given by

$$g_0 = \rho\sigma = l^{-1}. \tag{12}$$

Following the theory of Aki and Chouet (1975), we can rewrite the coda decorrelation in terms of the scattering coefficient (g_0) between a perturbed (p) and unperturbed (u) medium (Zotz-wilson et al., 2020).

$$K(t) = \frac{v_0}{2} t \ \left|\Delta g_{0_{p-u}}\right|, \tag{13}$$

where $K(t)$ is the theoretical decorrelation coefficient, t the time in the coda, and v_0 the velocity in the medium. Using a rolling reference ($N = 1$), the changes in the absolute value of $|g_0|$ are monitored as a rate of change (e.g., Zotz-Wilson et al., 2020).

3. Results

3.1. Fault Slip Behavior

From the principal stresses, increasing fluid pressures, and area of the fault plane, the evolution of friction coefficient μ is estimated for the saw-cut samples (Equation 1, Figures 5a, 5c, 6a, and 6c). It is assumed that the whole fault plane accommodates slip in each event (see a zoomed view of a single step in Figures 6a and 6c). As μ increases during fluid pressurization, frictional strengthening is visible for the two different injection patterns (shaded green in Figure 6). At the onset of fault reactivation, μ deviates from linearity (start of yellow shaded area in Figure 6) and drops (shaded red in Figure 6), simultaneously with the shear stress, when the fault slips. During each slip event (red shaded areas in Figures 6 and 8), the slip velocity rapidly accelerates to a maximum sliding velocity. Stick-slip events with peak slip velocities below 1 mm/s are defined as slow stick-slip events (L. Wang et al., 2020). The maximum slip velocities observed are <6.5 μm/s, therefore all recorded slip events in these experiments are slow stick-slip. This slow-slip is regarded as co-seismic slip, as there is still radiation of elastic

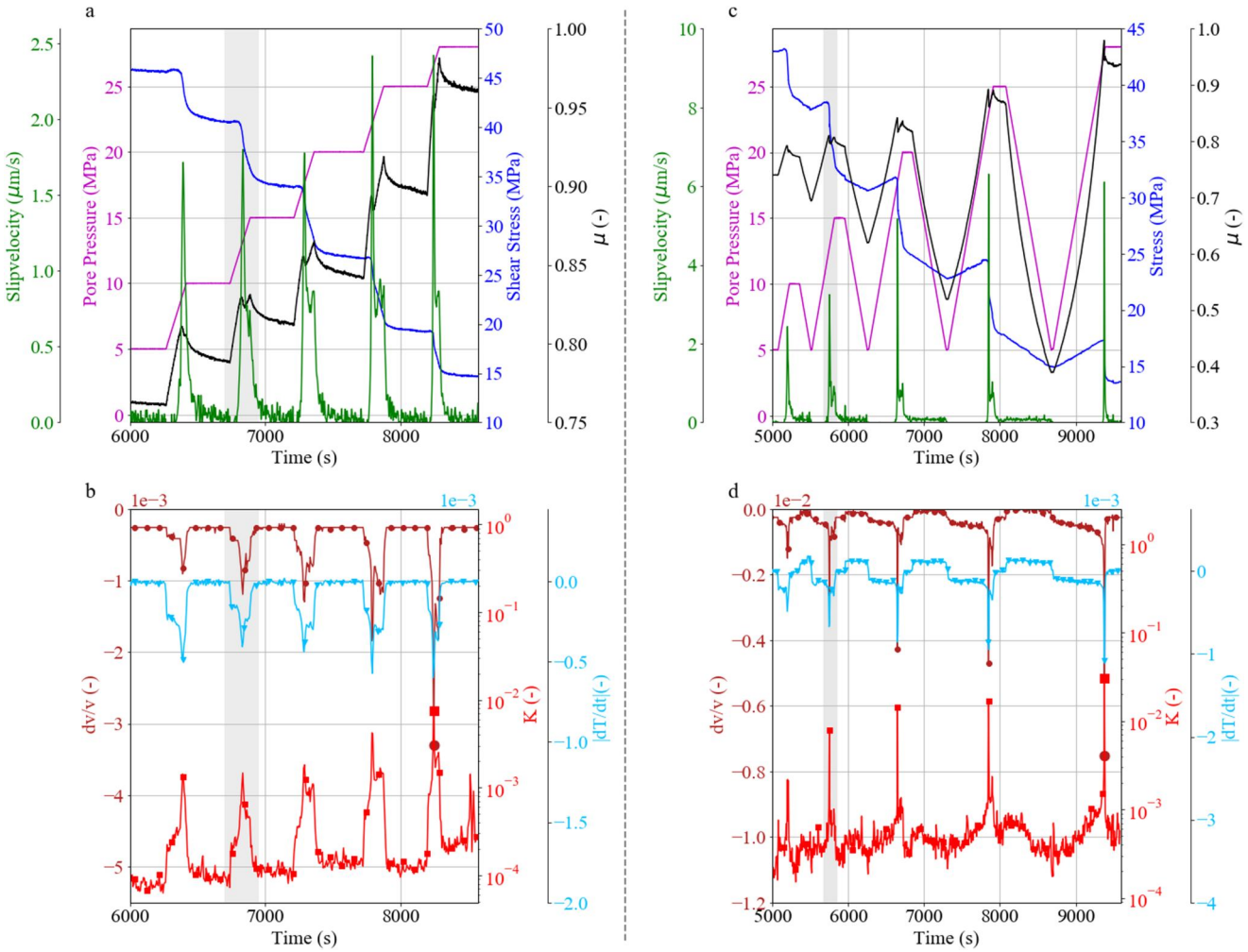

Figure 5. Evolution of mechanical and acoustic parameters during the reactivation of the saw-cut samples. (a and b) Shows the results of the stepwise injection experiment. (c and d) Shows the results of the cyclic injection experiment. (a and c) Shows the evolution of the shear stress τ, friction coefficient μ, and slip velocity along the fault due to increasing pore pressure. (b and d) Shows the derivative of the transmissivity T and the evolution of coda wave parameters K and dv/v. Slip event shaded in gray zoomed view visible in Figure 6.

waves (Veltmeijer et al., 2023a; L. Wang et al., 2020; Ye & Ghassemi, 2020). After reactivation of the fault, μ continues to increase with continued fluid pressurization (shaded blue in Figure 6). During this stage, μ is not affected by fault slip, as the fault continues to slip with low background velocities of ≈0.8 μm/s. At the end of each injection step, a gradual drop of μ indicates sample relaxation. During the rest in between injection periods, the slip velocity drops to creep velocities near zero ($<0.1 \times 10^{-3}$ μm/s), until a new injection stage starts.

In general, the rough fault exhibits very similar behavior during cyclic injection (Figures 3c, 3d, 4c, and 4d). However, during cyclic injection, the slip events show larger and more abrupt drops in τ, μ, and peaks in slip velocity. But after the slow stick-slip event, similar low background velocities of ≈0.8 μm/s are recorded, and in between injection events the rates drop to near zero as well.

The exact area of slip in the rough fault and how it changes during slip is unknown, therefore the evolution of the friction coefficient on the rough fault can't be estimated. However, using the evolution of shear stress and displacement, we can still observe the following. Slow slip is observed along the fault plane with peak velocities well below the velocities observed for slip on a saw-cut fault (Figure 9). After the slow slip event reactivation (shaded red in Figure 8), sample relaxation causes the slip velocity to drop to creep velocities near zero ($<0.1 \times 10^{-3}$ μm/s) until a new injection stage starts, similar to the saw-cut faults (Figure 8). Also on rough faults, the slip velocities are again higher for cyclic than for step-wise injection, however, the difference is less

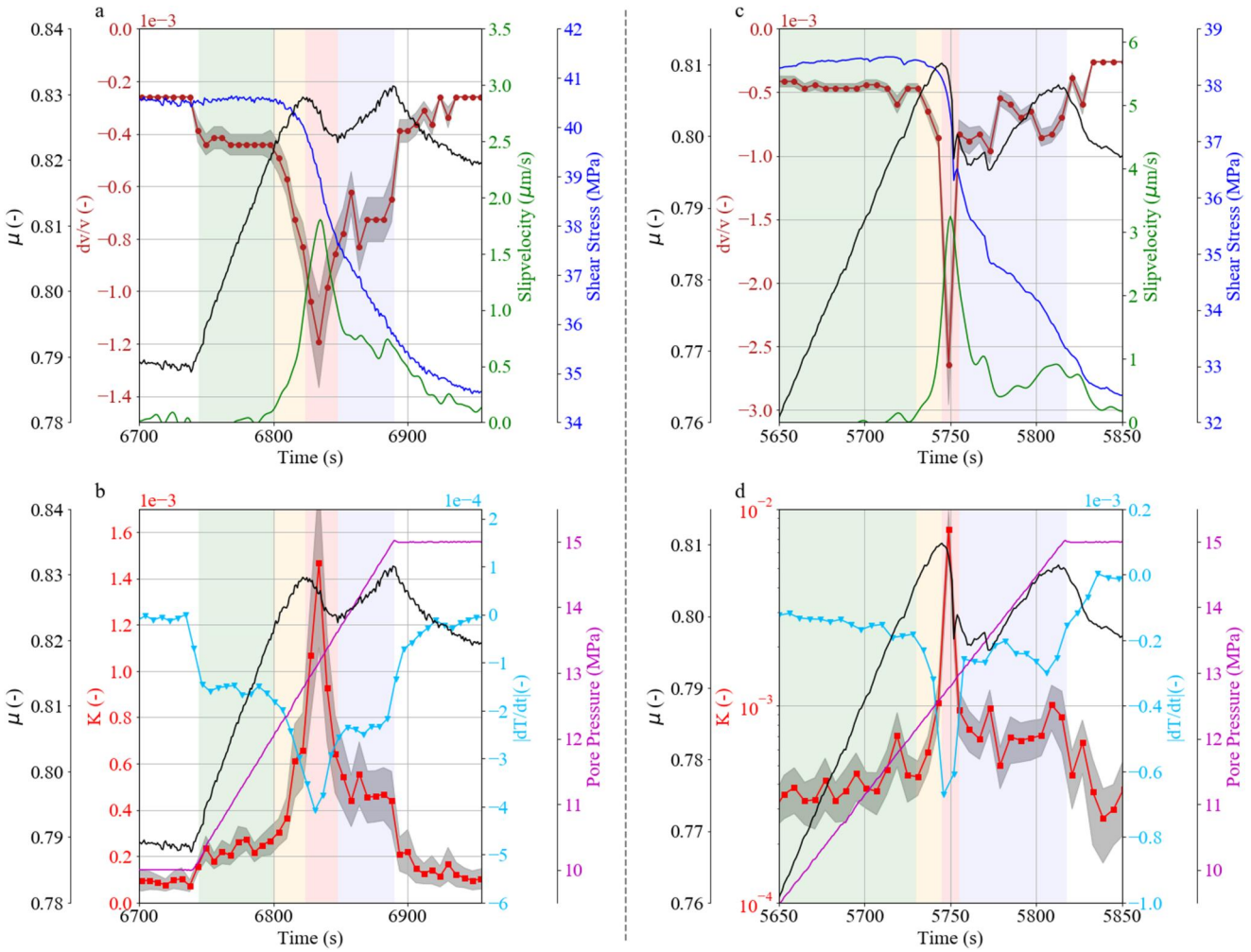

Figure 6. Zoom of single slip events (shaded gray in Figure 5) (a and b) showing the evolution of mechanical and acoustic parameters during the reactivation of the saw-cut samples of the second slip event induced by stepwise injection experiment and (c and d) the second slip event induced by cyclic injection experiment. The shaded gray around the decorrelation coefficient *K* shows the standard deviation and the colored shaded areas in figures (a)–(d) indicate the four stages of fault reactivation, green: inter-seismic stage, yellow: pre-seismic stage, red: co-seismic stage, and blue: post-co-seismic stage.

substantial than observed for slip along the saw-cut fault (Figure 9). During the last stepwise injection step a large stress drop occurred, and when taking the sample out it had an additional fracture. Therefore, the last step of the stepwise injection needs to be disregarded in the fault slip analysis.

3.2. (Micro-) Structural Observations

The fault plane of samples shows damage after the reactivation experiments. Most of the gouge forms during fault slip, due to shear slip, significant grain size reduction took place, resulting in fault gouge formation (Figure 3). During sliding, the quartz grains at the surface are crushed, and the resulting gault gouge coats the fault plane upon post-experimental sample retrieval.

In the sawcut experiments, the contact of the fault plane can be considered relatively smooth and a single contact in macro-scale. On the micro-scale, however, each single grain contact acts as an asperity. This is also shown by the gouge which is distributed heterogeneously on the fault surface, suggesting that even the relatively smooth surface of the saw-cut still has heterogeneous frictional properties across the fault (Figure 3). Each experiment comes out with its own distinct pattern of gouge distribution, without obvious correlation to the experimental parameters.

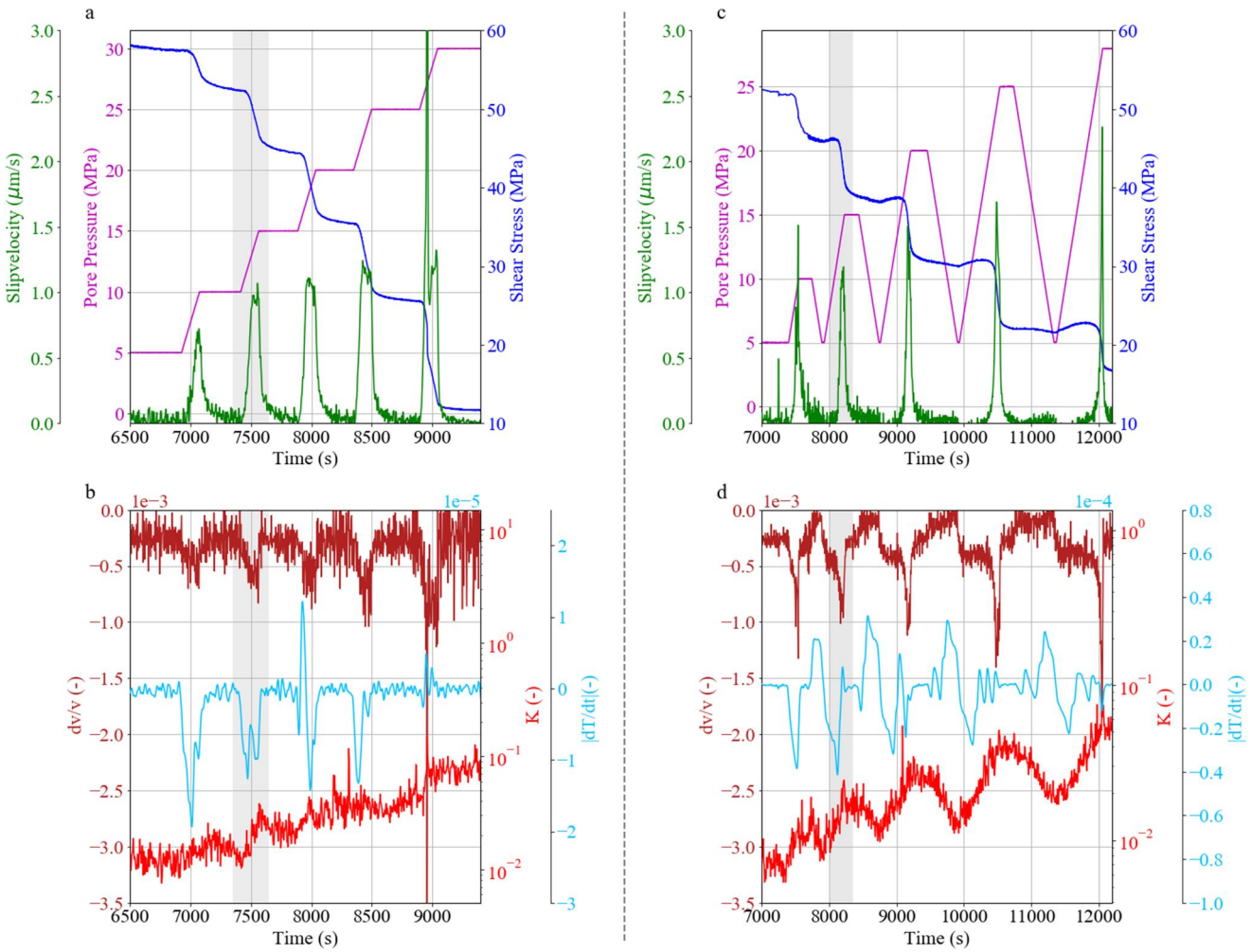

Figure 7. Evolution of mechanical and acoustic parameters during the reactivation of fractured samples, or rough fault. (a and b) Shows the results of the stepwise injection experiment. (c and d) Shows the results of the cyclic injection experiment. (a and c) Shows the evolution of the shear stress τ, friction coefficient μ, and slip velocity along the fault due to increasing pore pressure. (b and d) The derivative of the transmissivity T and the evolution of coda wave parameters K and dv/v. The slip event is shaded in gray, zoomed view visible in Figure 8.

After finishing the experiment with a rough fault experiments, a CT image (Figure 11) was made to show slices of the fault plane after finishing the experiment. Along the fault plane, black areas are visible, indicating open pore space. There are also intermediately shaded gray areas, where the fault plane is harder to track. Image segmentation by simple thresholding shows the approximate 3D view of the fault plane. It shows a very irregular fault surface (Figure 12c), which forms a stark contrast to the simple and straight saw-cut planes.

3.3. Ultrasonic Monitoring

We first describe the results of the saw-cut experiments. Monitoring the evolving the transmissivity T, a measure of the transmitted amplitude, was previously used by Nagata et al. (2008) and Shreedharan et al. (2021a) to track fault properties in direct shear experimental setting, without considering the effects of pore pressure. It is known that pore pressure has a large effect on the transmission of wave energy (Winkler & Nur, 1979). This is also observed in this set of experiments, in which was observed that transmitted amplitudes decrease and increase inversely with pore pressure. To investigate the more subtle changes due to fault reactivation, the derivative of T is plotted (Figures 5b, 5d, 6b, and 6d). This shows that during fault slip there is an accelerated drop in the transmitted amplitude. During each slip event the sample is shortened, decreasing the direct travel path of the wave, which should increase the amplitude. However, the transmissivity decreases with each injection step instead, and exhibits a faster rate during slip. We observed gouge formation during experiments with slip. Theoretically, a

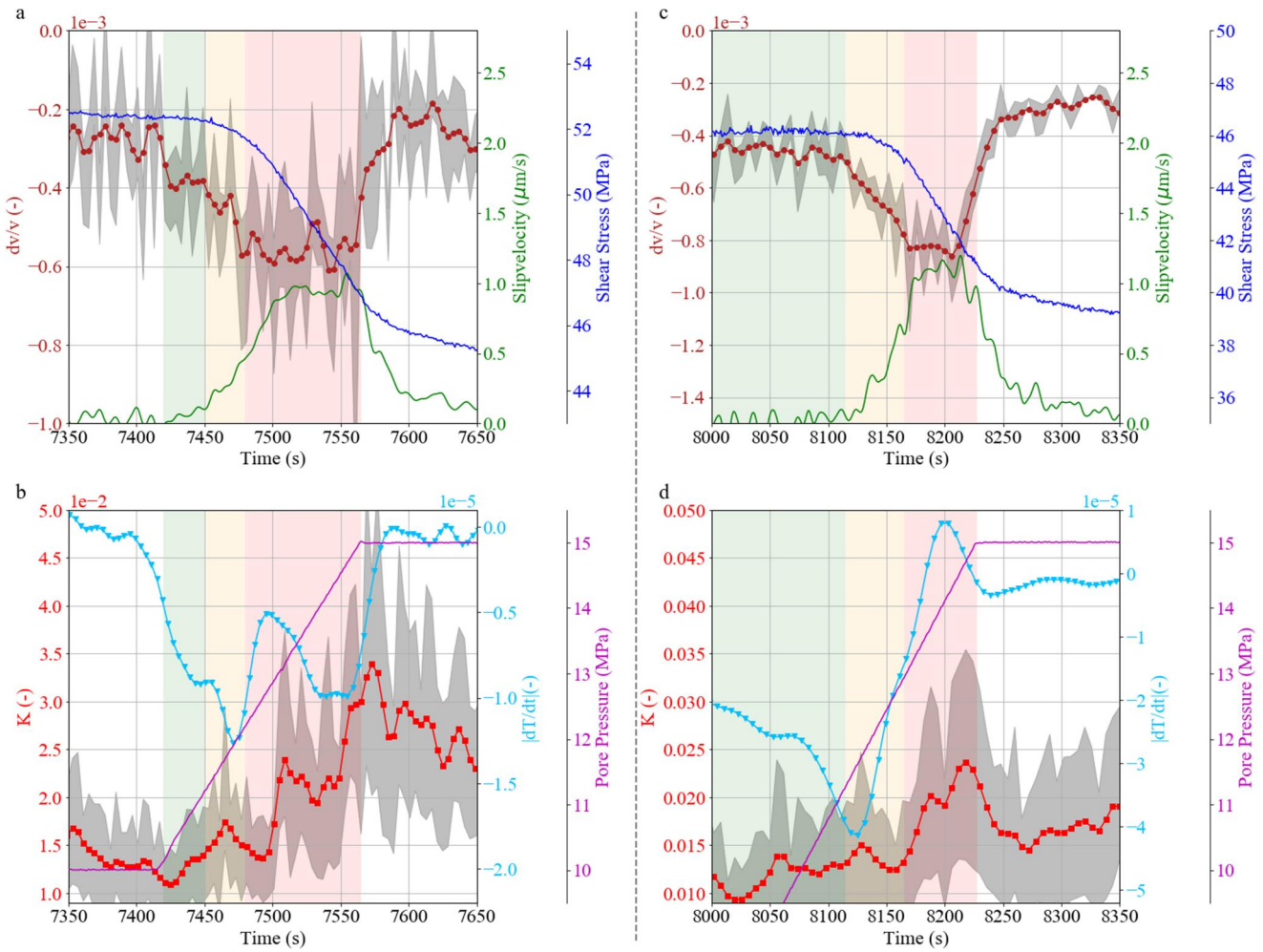

Figure 8. Zoom of single slip events (shaded gray in Figure 7). (a and b) Showing the evolution of mechanical and acoustic parameters during the reactivation of fractured samples, or rough fault of the second slip event induced by stepwise injection experiment and (c and d) the second slip event induced by cyclic injection experiment. The shaded gray around the decorrelation coefficient *K* shows the standard deviation and the colored shaded areas in figures (a)–(d) indicate the four stages of fault reactivation, green: inter-seismic stage, yellow: pre-seismic stage, red: co-seismic stage.

thicker gouge layer should attenuate waveforms traveling through the sample more than a thinner gouge layer. Given that the transmissivity still shows a decrease during cyclic injection, even while the pore pressure was returned to the initial pressure and including the shortening of the sample due to slip, we infer this decrease to be due to additional attenuation by ongoing gouge formation.

The small stress variations along the fault plane are interpreted and assessed by comparing the coda of the recorded wave fields, where a moving reference wavefield was used (t_{N-1}–t_N). Therefore the decorrelation coefficient *K* and velocity change *dv*/*v* are monitored as a rate of change. Coda wave parameters *K* and *dv*/*v* respond to fluid injection, and increase and decrease in conjunction with the injection pattern, showing their sensitivity to stress perturbation on the sample scale (Figures 5b, 5d, 6b, and 6d). Within this background response to the change in sample stress during injection, another trend is visible. The evolution of coda wave parameters *K* and *dv*/*v* show a strong correlation to the slip velocity, with an accelerating increase before slip (yellow shaded areas in Figure 6), an obvious peak during slip (red shaded areas in Figure 6), and a reduction to background levels at moments of relaxation. The magnitude of these peaks increases per cycle (Figures 5b and 5d) similar to the slip velocity (Figures 5a and 5c). This indicates that *dv*/*v* and *K* are indeed sensitive to the slip velocity along the saw-cut fault plane. As fault slip is a result of stress changes and the resulting loss of asperity contact along the fault plane, we infer the changes in *dv*/*v* and *K* are results of changes in fault contact on the microscale. *T* shows a similar trend to *dv*/*v,* showing an equivalent sensitivity to the stress changes along a saw-cut fault.

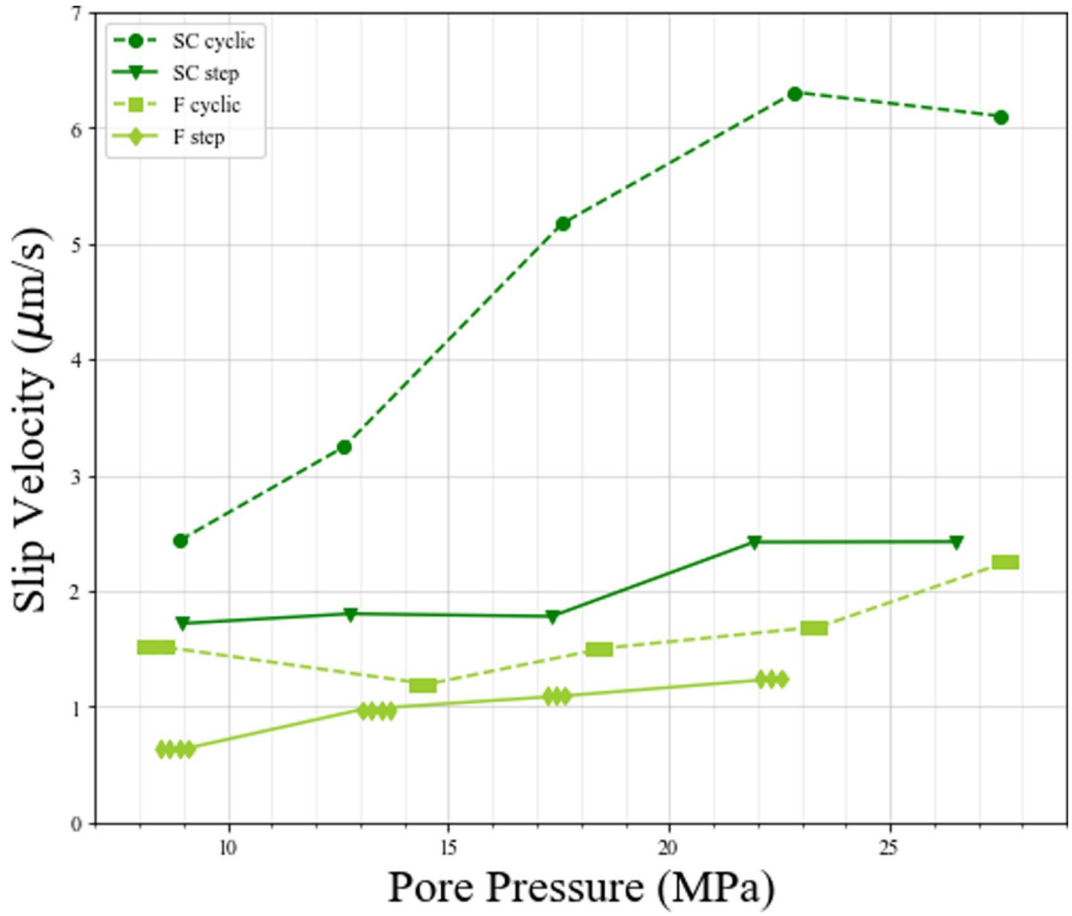

Figure 9. Peak slip velocity for each injection (stepwise and cyclic) step for the saw-cut (SC) and fractured (F) samples. The co-seismic phase for the rough fault (fractured samples) is more prolonged, the markers show the potential start of the co-seismic phase whereas in the SC samples the peak in velocity coincides with the co-seismic phase.

Moving to the more complex situation of the rough fault, we observe that for the rough fault, the *T* pattern changes per slip event (Figures 7b and 7d). Rather than decreasing amplitudes prior to slip (Figures 6b and 6d), increasing amplitudes in the transmitted waves are observed during and just before slipping along the rough fault (Figures 7b and 7d). A similar observation can be made for coda parameter *K* (Figures 7b, 7d, 8b, and 8d). The scattering along the more uneven slip along the rough fault causes an incoherent signal from the decorrelation coefficient *K* (Figures 7b and 7d). While the general sample scale pattern of fluid injection is still visible (Figure 7d), the more subtle trend with accelerated increase during fault reactivation (observed in the saw-cut faults; shaded yellow in Figures 6b and 6d) is lost by the more complicated slip along the rough fault plane (Figures 7b and 7d). Nonetheless, the velocity change dv/v, however, is still showing the same trends with slip velocity (Figures 8a and 8c). This suggests that the velocity change obtained by the coda wave, which sampled the fault, still is a promising indicator for the pre-slip and slip phase along the rough fault plane (shaded yellow and red respectively in Figures 8a and 8c).

4. Discussion

In the following, we will discuss the effect of injection pattern on fault reactivation and measured waveforms. Then we go on to discuss the difference of the effectiveness of ultrasonic monitoring for smooth versus rough faults, where we presume that the type of roughness created by the faulting procedure is more representative for in situ roughness. Following, we will discuss the added benefit of using coda wave interferometry to determine precursors to fault reactivation, and finally, we will discuss the implications of our results for earthquake forecasts.

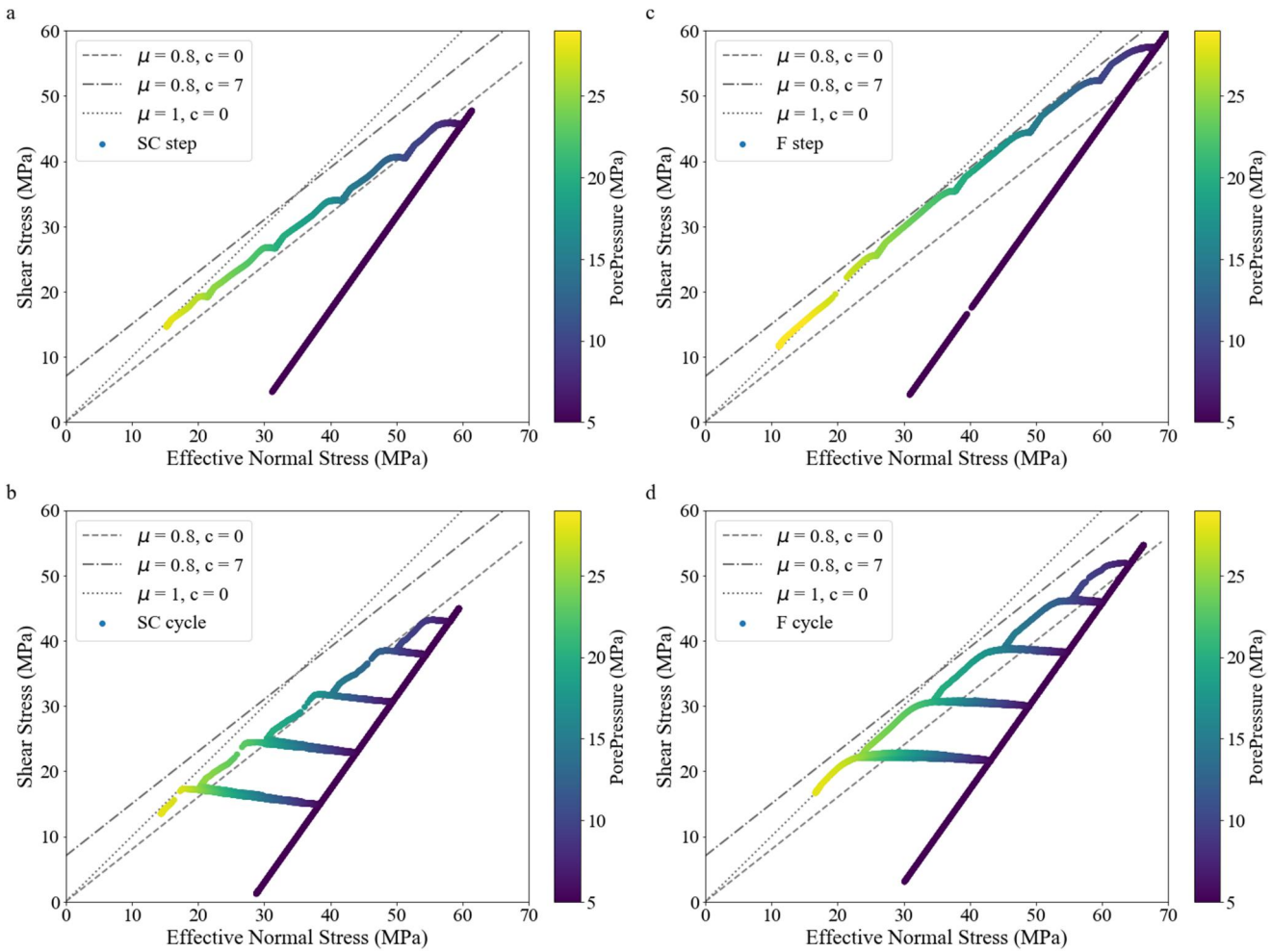

Figure 10. Showing the relation between the principal stresses on the fault plane "color coded" by the applied pore pressure; (a) for the saw-cut stepwise injection experiment; (b) for the saw-cut stepwise cyclic experiment; (c and d) for the fractured samples stepwise and cyclic injection protocol respectively. Indicative failure envelopes are drawn for failure planes with friction coefficient μ is 0.8 or 1 and cohesion c is 0 or 7.

4.1. Effect of Injection Pattern

By stepping or cycling the pore pressure, fault instability is reached multiple times. In each cycle or step, when pore pressure stops increasing, we allow the system to re-stabilize and reach a new equilibrium. By reducing the pore pressure each cycle, the fault plane can relax and build strength caused by the compaction of the fault due to an increased effective normal stress (Figure 10). In cycles where pore pressure is reduced the fault compacts further, and subsequently, more energy is needed to reactivate the fault. This corresponds to an increase in the fault energy release, as observed by increasing slip velocities in cyclic injection (Figure 9).

In the faulted samples, the grains on the fault surface are crushed during sliding and pressuring of the fault, creating a gouge layer along the fault surface. This changes the fault properties like the friction coefficient, which in the quartz-rich Red Felser sandstone, would be expected to have a frictional strengthening effect (Bakker et al., 2016; He et al., 2013). We do observe continuous restrengthening of the fault throughout the experiment (Figure 10). Most of the gouge is expected to form just prior to and during fault slip, when we expect to have the highest local stresses on the asperities and movement, causing the observed grain size reduction (Figure 3). Seismic waves are increasingly attenuated and scattered due to the gouge formation and due to the changes in stress and movement and repositioning of the scatterers along the fault. These changes were used as a precursor to fault reactivation during ultrasonic monitoring.

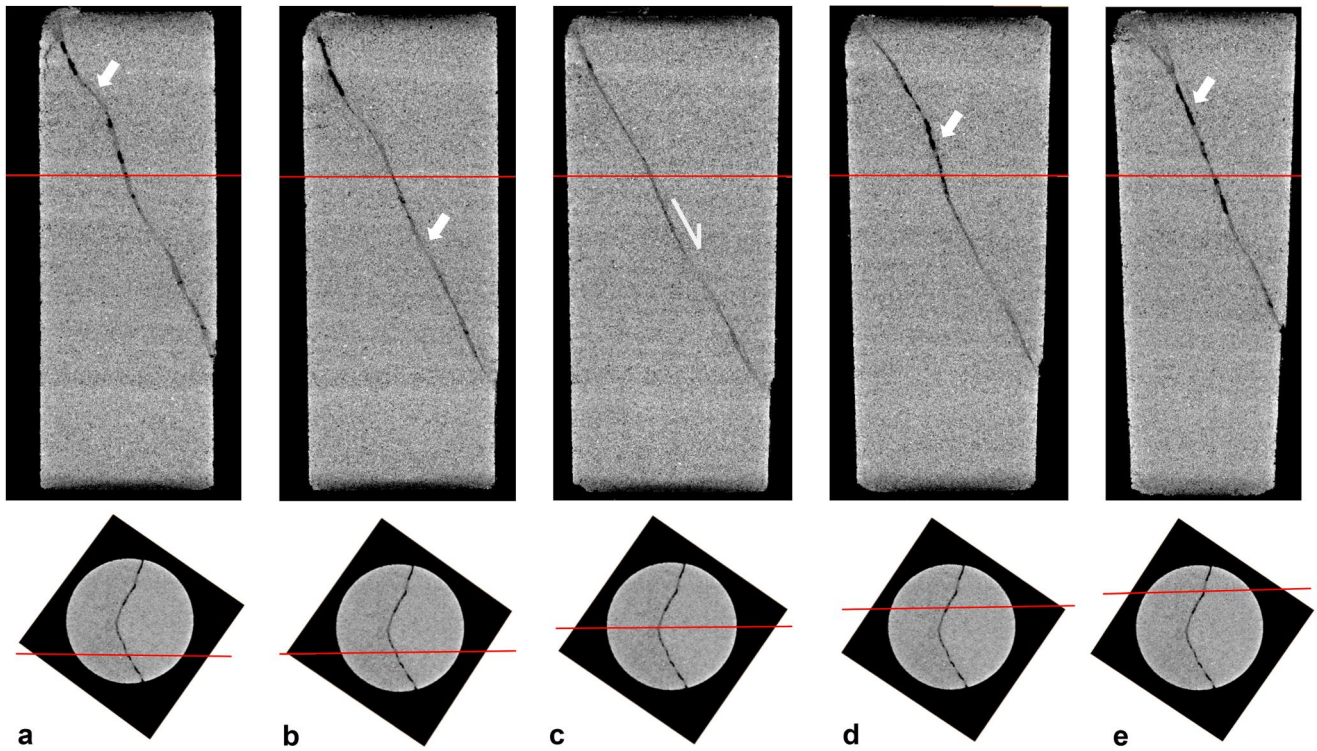

Figure 11. CT sections cutting through the fault plane, showing the irregular shape of the rough fault plane. Arrows point at the black areas, which indicate areas of more pore space, hence opening of the fault, and to more greyish blurry areas, which show the interlocking and compaction areas along the fault. The red lines show the horizontal and vertical position of the slices. The movement along the fault plane is caused by downward sliding of the top half of the sample. The white arrows indicate areas of compaction (a and b) and areas of opening (d and e). The direction of movement is indicated in (c).

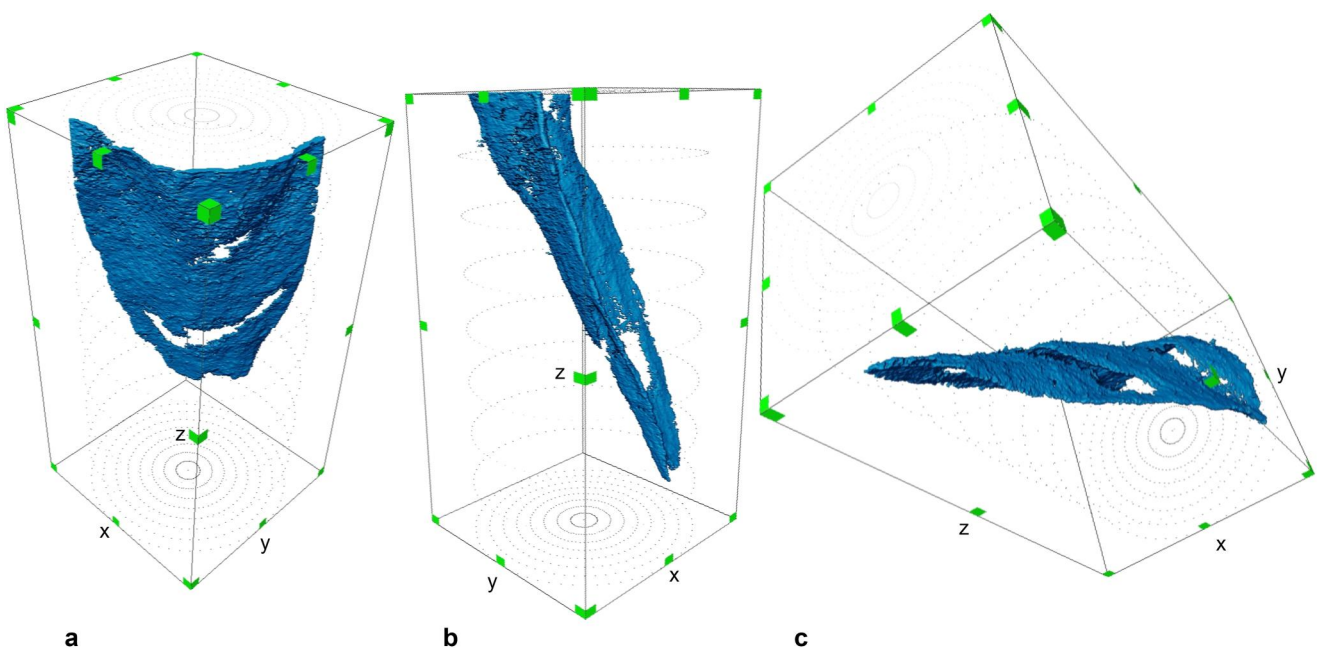

Figure 12. Image of the fault area, extracted from the CT images. This shows the irregular shape of the rough fault plane. The gaps are stronger compaction areas of fault, which weren't picked up in processing of the fault area in the CT scans. (c) Shows a jump in the fault plane after an area of compaction.

The peaks of decorrelation coefficient K, a proxy for the scattering coefficient (Equations 12 and 13), during slip can be explained by an increased addition of scatterers, caused by the fracturing, crushing and movement of the grains along the surface area of the fault plane forming a progressively thicker gouge layer. The creation of this layer along with stress release during slip also causes the drop in velocity dv/v, and the transmitted amplitude T during fault reactivation. Both parameters peak during fault slip, afterward they are fluctuating around a constant rate, similar to the observed constant slow slip (Figures 5b and 5d). The slow stick-slip events induced by cyclic injection have a greater amplitude and are more abrupt than for stepwise injection due to a greater release of fault energy (Figures 5b, 5d, 6b, and 6d). This results in larger amplitudes in the coda wave parameters K and dv/v, but also fewer sampling points per slip event.

4.2. Effect of Roughness

The roughness of the fault plane illustrated by the CT image (Figure 11), implies the fault plane has multiple areas of compaction (Figures 11a and 11b), where interlocking of asperities can occur, and areas of opening (Figures 11d and 11e). During slip, parts of such a rough fault can lock, and the fault will locally compact, whereas it will dilate locally there where the two halves move apart. Both phenomena could enhance resistance to shear along the fault by interlocking asperities or dilatant hardening (Rudnicki & Chen, 1988). This increased cohesion of the fault (Figures 10b and 10d) and resistance to shear result in more prolonged slow slip (Figures 8a and 8c) upon reactivation until the fluid injection is stopped in which we observe fluctuating slip velocities, suggesting the overcoming the interface locking. In contrast, the saw-cut fault is smooth and could therefore slip more easily in its entirety once fault instability is reached. Accordingly, we observe higher slip velocities (Figure 9) upon reactivation and a short and larger stress drop (Figures 6a and 6c), indicating short and fast reactivation with afterward continuous slow slip phase due to continued elevated pore pressure and reduced effective normal stress reducing the interface locking along the smooth fault (Alghannam & Juanes, 2020).

The effect of compaction and dilation along the rough fault can be discerned in the ultrasonic data. Compaction will cause increasing acoustic amplitudes, whereas dilation causes more attenuation of the waves and lower transmissivity. This interpretation is consistent with the systematic differences in the increasing and decreasing behavior of T prior to fault reactivation (Figures 7b and 7d) of the rough fault. Where the decreasing behavior of T during fault reactivation of the smooth fault (Figures 5b and 5d) suggests the detection of dilation along the fault plane, its increase suggests the detection of compaction. The scattering along the more uneven slip along the rough fault causes a more incoherent signal from the K (Figures 7b and 7d). While the general pattern of fluid injection is still visible (Figure 7d), the more subtle trend of fault reactivation is lost by the more complicated slip along the rough fault plane (Figures 8b and 8d). Cartwright-Taylor et al., 2022 described crack rotation with antithetic slip as an additional mechanism for local stress rotation and slip, allowing shear along more unfavorably orientated faults, which among fracturing and crushing of the grains influence the scattering, therefore causing a more incoherent K compared to sliding along the smooth fault surface, where we won't expect this fault rotation and antithetic slip.

4.3. Precursors to Fault Reactivation

The direct shear experiments by Shreedharan et al. (2021a, 2021b) suggest a physical connection between ultrasonic evolution (amplitude and direct wave velocity) and variations in healing, pre-slip driven asperity changes, and shear stiffening of wallrock. Their results, similar to ours, suggested as well that the destruction of asperities and increase in fracture density due to stress changes along the fault during and prior to fault slip is expected to result in reduction in transmitted amplitude T and P-wave velocity. However, the work done by Shreedharan et al. (2021a, 2021b) lacked the additional layer of complexity introduced by the presence of pore pressure variations. Research by Passelègue et al. (2018) and Winkler and Nur (1979), indicates that ultrasonic amplitude and velocity are influenced by pore pressure. In this study and in Veltmeijer et al. (2022), we observe that pore pressure increases have a large effect on the transmitted amplitude, emphasizing the importance of considering relative changes in transmissivity to infer the nuance introduced by small variations in healing and interface locking along the fault.

The presented slip velocities can be categorized as slow slip (<6.5 μm) or creeping velocities ($<0.1 \times 10^{-3}$ μm) (Figures 5 and 7). These velocities are commonly thought to be aseismic. However, experiments shown by L. Wang et al. (2020), Ye and Ghassemi (2020), and Veltmeijer et al. (2023a) show recorded micro seismic events

with similar slow slip velocities. Hence, some seismic energy has been released, and we will characterize the fault reactivation according to the fault reactivation stages (Figure 1) (Shreedharan et al., 2021a). By analyzing the temporal evolution of the coda waves, stress changes on the fault surface can be identified, demonstrating the potential of coda waves to identify the stages of fault reactivation: inter-seismic phase: linear stress build-up, the pre-seismic phase: early creep/pre-slip, the co-seismic phase: stress drop and a continuous sliding phase for the saw cut fault planes followed by a post-seismic phase at the end of injection: fault healing (i.e., following the terminology and sequence shown in Figure 1). Our results show that we can identify the pre-seismic phase of laboratory injection-induced fault slip. By zooming on a single step or cycle, the K, dv/v, and T can be used to identify the different stages of reactivation. dv/v reaches a new equilibrium after the start of injection (Figures 6 and 8), this can also be observed in the K and T for the reactivation of the saw-cut fault. The linear stress build up along the fault causes a constant drop in velocity following the fluid pressure identifying as the inter-seismic phase (green shaded area in Figures 6 and 8). Once the fault plane starts to become unstable in the pre-slip phase (yellow shaded area in Figures 6 and 8) the dv/v, K, and T show an accelerated decrease/increase in values (Figure 6) peaking at the co-seismic stage (red shaded area in Figures 6 and 8). These early changes in values deviate from the change caused by increased pore pressure and are hence a proxy of the stress change along the fault plane. Detecting the pre-slip phase could be a first step for forecasting the upcoming fault reactivation as it is an indication of the upcoming co-seismic slip phase.

The drop in dv/v occurs over a narrow range, as well as the standard deviation indicated in gray, hence it gives a fairly accurate indication of both the preparatory phase and fault reactivation (Figure 6b). Due to the smooth fault, the stress release and fault reactivation are rapid, and hence the preparatory phase is short. To reactivate the rough fracture, more energy is needed, as some parts of the fracture aren't favorably oriented to move (Figure 11). During this extended preparatory phase, the drop in velocity remains clear and shows the same pattern (Figure 6d), albeit more noisy one due to the more complex fault area. Using CWD, the scattering coefficient K, a proxy for grain crushing or movement, is determined. This K clearly indicated the saw-cut fault reactivation, however, when the fault plane becomes more complex, the K seems to be of little use in detecting both the preparatory phase and fault reactivation (Figures 8c and 8d). A similar conclusion can be drawn from the transmissivity. T in the rough fault initially showed similar patterns to the saw-cut fault reactivation for the first injection step/cycle, but the later steps differ. Even though monitoring of fault reactivation is more complex, and the signal is noisier for the rough fault, using the dv/v, the pre-slip and co-seismic phase of fault reactivation can still be determined. Due to the more prolonged pre-slip phase, the forecast of the co-seismic stage can be done relatively earlier as higher differential stresses are needed to reactivate the rough fault.

After the co-seismic stage, post-slip sliding is observed in the saw-cut reactivated faults. As the fault remains prone to sliding due to continued fluid injection the fault plane continues to slowly slip until fluid injection ends (Figure 6). No post-slip during the injection is observed as the rough fault continues to slip slowly (Figure 8), rather than showing a short and rapid co-seismic phase (as happened for the smooth fault). Once injection stops, the fault is not perturbed anymore, which signifies the start of post-seismic phase, during which the fault relaxes and can heal until the next step in the injection protocol starts.

4.4. Implications for Induced Seismicity

In our constrained laboratory setting, we accurately identified the pre-slip phase using a combination of parameters, including transmitted amplitude, and CWI parameters, highlighting that velocity changes obtained from coda offer more precision in complex situations compared to the amplitudes. This suggests the potential inclusion of coda wave interferometry in forecasting fault reactivation, presenting an improvement for input in forecasting models. Efforts, including machine learning models, have been made to improve predictions of lab quakes (Laurenti et al., 2022; Rouet-Leduc et al., 2017; K. Wang et al., 2022), also including transmitted amplitudes to the models (Shreedharan et al., 2021b).

Upscaling these findings to real reservoir remains a challenge, even though pre-seismic crustal velocity anomalies have been observed for a limited number of earthquakes (Chiarabba et al., 2020; Niu et al., 2008). More work is needed to verify the usefulness of the results for upscaled fault zone length, maturity, time, and complexity and extent of the damage zone. From the engineering perspective it would require work on placement of monitoring stations and monitoring frequency. Due to the fast nature of fault reactivation in the laboratory, with pre- and co-seismic phases lasting seconds, monitoring points during the pre-slip phase are limited due to equipment

constraints. Nevertheless, assuming a one-to-one relationship between the laboratory and field scale, we do see potential in this method for monitoring fault reactivation. In the laboratory, the pre-slip phase spans only a few seconds, equivalent to a 5 MPa increase in pore pressure (or a 5 MPa decrease in effective stress). Extrapolating this to the field, a similar pore pressure change may take several days to weeks or more to build up after which reactivation occurs. This potentially would allow more time for measurements and forecasting. Our work is performed in a carefully constrained laboratory setting, and does not take in account temperature, maturity or forward prediction of fault reactivation. We encourage future experimental research in these directions as well as upscaling and field applicability.

5. Conclusions

In this paper, we aim to monitor fluid-induced fault slip in laboratory experiments more accurately and understand the connection between precursors and mechanisms of failure. By analyzing the temporal evolution of the coda waves and seismic amplitudes, stress changes on the fault surface can be identified, demonstrating the potential of coda waves to identify the stages of fault reactivation as a possible basis for forecasting injection-induced fault-slip. The precursory signals obtained by coda wave interferometry and decorrelation are compared for both a smooth saw-cut and rough fault.

It is shown that the CWI velocity change is most sensitive to the pre-slip phase and fault reactivation. However, as all the compared attributes are obtained from the same wavelet a combination of these properties shows that the stress changes along the fault can be inferred with more accuracy. As a result, the combination may be useful for monitoring faulted or critically stressed reservoirs that experience pore pressure changes.

The coda analysis and amplitudes are used to identify the different stages in the laboratory seismic cycle, as precursors to fault slip and to give insight into reactivation mechanisms. Showing ultrasonic monitoring techniques can be used to detect the different fault reactivation stages: inter-seismic phase: linear stress build-up, the pre-seismic phase: early creep/pre-slip, the co-seismic phase: stress drop and a continuous sliding phase for the saw cut fault planes followed by a post-seismic phase at the end of injection: fault healing.

Our experiments demonstrate the feasibility of active ultrasonic monitoring as a tool to identify precursors to laboratory fluid-induced earthquakes. While these experiments show the feasibility of the active monitoring method in a controlled environment in the laboratory, and its potential to infer the pre-seismic phase, it does not yet include the forward forecasting. The timing of the pre-phase, from detection to forward forecasting and the added complexity from lab to field-scale should still be studied. The potential to infer aseismic stress changes pointing toward seismicity from active ultrasonic campaigns could be of added value to monitoring and forecasting (models).

Data Availability Statement

The laboratory facilities at TU Delft were used to perform the experiments and record the data (loading data and waveforms) used in this publication. This data is accessible at the 4TU.ResearchData repository under a CC BY 4.0 license. https://doi.org/10.4121/21557910 (Veltmeijer et al., 2023b).

Acknowledgments
This research was (partially) funded by NWO Science domain (NWO-ENW), project DEEP.NL.2018.048.

References

Aki, K., & Chouet, B. (1975). Origin of coda waves: Source, attenuation, and scattering effects. *Journal of Geophysical Research*, *80*(23), 3322–3342. https://doi.org/10.1029/jb080i023p03322

Alghannam, M., & Juanes, R. (2020). Understanding rate effects in injection-induced earthquakes. *Nature Communications*, *11*(1), 1–6. https://doi.org/10.1038/s41467-020-16860-y

Bakker, E., Hangx, S. J. T., Niemeijer, A. R., & Spiers, C. J. (2016). Frictional behaviour and transport properties of simulated fault gouges derived from a natural CO_2 reservoir. *International Journal of Greenhouse Gas Control*, *54*, 70–83. https://doi.org/10.1016/j.ijggc.2016.08.029

Barnhoorn, A., Verheij, J., Frehner, M., Zhubayev, A., & Houben, M. (2018). Experimental identification of the transition from elasticity to inelasticity from ultrasonic attenuation analyses. *Geophysics*, *83*(4), MR221–MR229. https://doi.org/10.1190/geo2017-0534.1

Byerlee, J. D. (1967). Frictional characteristics of granite under high confining pressure. *Journal of Geophysical Research*, *72*(14), 3639–3648. https://doi.org/10.1029/JZ072i014p03639

Cartwright-Taylor, A., Mangriotis, M. D., Main, I. G., Butler, I. B., Fusseis, F., Ling, M., et al. (2022). Seismic events miss important kinematically governed grain scale mechanisms during shear failure of porous rock. *Nature Communications*, *13*(1), 6169. https://doi.org/10.1038/s41467-022-33855-z

Chiarabba, C., De Gori, P., Segou, M., & Cattaneo, M. (2020). Seismic velocity precursors to the 2016 Mw 6.5 Norcia (Italy) earthquake. *Geology*, *48*(9), 924–928. https://doi.org/10.1130/G47048.1

Dempsey, D., & Suckale, J. (2017). Physics-based forecasting of induced seismicity at Groningen gas field, the Netherlands. *Geophysical Research Letters*, *44*(15), 7773–7782. https://doi.org/10.1002/2017GL073878

Eradus, D. (2019). *Petrographical description and petrophysical measurements on the Red Felser sandstone*. Delft University of Technology.

Frank, S., Heinze, T., & Wohnlich, S. (2020). Comparison of surface roughness and transport processes of sawed, split and natural sandstone fractures. *Water (Switzerland)*, *12*(9), 2530. https://doi.org/10.3390/w12092530

Geller, R. J. (1997). Earthquake prediction: A critical review. *Geophysical Journal International*, *131*(3), 425–450. https://doi.org/10.1111/j.1365-246x.1997.tb06588.x

Grêt, A., Snieder, R., & Scales, J. (2006). Time-lapse monitoring of rock properties with coda wave interferometry. *Journal of Geophysical Research*, *111*(3), 1–11. https://doi.org/10.1029/2004JB003354

Guglielmi, Y., Cappa, F., Avouac, J. P., Henry, P., & Elsworth, D. (2015). Seismicity triggered by fluid injection-induced aseismic slip. *Science*, *348*(6240), 1224–1226. https://doi.org/10.1126/science.aab0476

Gulia, L., Wiemer, S., & Vannucci, G. (2020). Pseudoprospective evaluation of the foreshock traffic-light system in Ridgecrest and implications for aftershock hazard assessment. *Seismological Research Letters*, *91*(5), 2828–2842. https://doi.org/10.1785/0220190307

He, C., Luo, L., Hao, Q. M., & Zhou, Y. (2013). Velocity-weakening behavior of plagioclase and pyroxene gouges and stabilizing effect of small amounts of quartz under hydrothermal conditions. *Journal of Geophysical Research: Solid Earth*, *118*(7), 3408–3430. https://doi.org/10.1002/jgrb.50280

Hough, S. E. (2009). *Predicting the unpredictable*. Princeton University Press. https://doi.org/10.1515/9781400883547

Kagan, Y. Y., & Jackson, D. D. (1991). Seismic gap hypothesis: Ten years after. *Journal of Geophysical Research*, *96*(B13), 21419–21431. https://doi.org/10.1029/91JB02210

Kaproth, B. M., & Marone, C. (2013a). Slow earthquakes, preseismic velocity changes, and the origin of slow frictional stick-slip. *Science*, *341*(6151), 1229–1232. https://doi.org/10.1126/science.1239577

Kaproth, B. M., & Marone, C. (2013b). Slow earthquakes, preseismic velocity changes, and the origin of slow frictional stick-slip. *Science*, *341*(6151), 1229–1232. https://doi.org/10.1126/science.1239577

Király-Proag, E., Zechar, J. D., Gischig, V., Wiemer, S., Karvounis, D., & Doetsch, J. (2016). Validating induced seismicity forecast models—Induced seismicity test bench. *Journal of Geophysical Research: Solid Earth*, *121*(8), 6009–6029. https://doi.org/10.1002/2016JB013236

Langenbruch, C., Weingarten, M., & Zoback, M. D. (2018). Physics-based forecasting of man-made earthquake hazards in Oklahoma and Kansas. *Nature Communications*, *9*(1), 1–10. https://doi.org/10.1038/s41467-018-06167-4

Larose, E., Planes, T., Rossetto, V., & Margerin, L. (2010). Locating a small change in a multiple scattering environment. *Applied Physics Letters*, *96*(20), 1–4. https://doi.org/10.1063/1.3431269

Laurenti, L., Tinti, E., Galasso, F., Franco, L., & Marone, C. (2022). Deep learning for laboratory earthquake prediction and autoregressive forecasting of fault zone stress. *Earth and Planetary Science Letters*, *598*, 117825. https://doi.org/10.1016/j.epsl.2022.117825

Main, I. G., & Meredith, P. G. (1989). Classification of earthquake precursors from a fracture mechanics model. *Tectonophysics*, *167*(2–4), 273–283. https://doi.org/10.1016/0040-1951(89)90078-4

Naderloo, M., Kumar, K. R., Hernandez, E., Hajibeygi, H., & Barnhoorn, A. (2023). Experimental and numerical investigation of sandstone deformation under cycling loading relevant for underground energy storage. *Journal of Energy Storage*, *64*, 107198. https://doi.org/10.1016/j.est.2023.107198

Nagata, K., Nakatani, M., & Yoshida, S. (2008). Monitoring frictional strength with acoustic wave transmission. *Geophysical Research Letters*, *35*(6), 1–5. https://doi.org/10.1029/2007GL033146

Niu, F., Silver, P. G., Daley, T. M., Cheng, X., & Majer, E. L. (2008). Preseismic velocity changes observed from active source monitoring at the Parkfield SAFOD drill site. *Nature*, *454*(7201), 204–208. https://doi.org/10.1038/nature07111

Noël, C., Passelègue, F. X., Giorgetti, C., & Violay, M. (2019). Fault reactivation during fluid pressure oscillations: Transition from stable to unstable slip. *Journal of Geophysical Research: Solid Earth*, *124*(11), 10940–10953. https://doi.org/10.1029/2018JB016045

Passelègue, F. X., Brantut, N., & Mitchell, T. M. (2018). Fault reactivation by fluid injection: Controls from stress state and injection rate. *Geophysical Research Letters*, *45*(23), 12837–12846. https://doi.org/10.1029/2018GL080470

Planès, T., Larose, E., Margerin, L., Rossetto, V., & Sens-Schönfelder, C. (2014). Decorrelation and phase-shift of coda waves induced by local changes: Multiple scattering approach and numerical validation. *Waves in Random and Complex Media*, *24*(2), 99–125. https://doi.org/10.1080/17455030.2014.880821

Planès, T., Larose, E., Rossetto, V., & Margerin, L. (2015). Imaging multiple local changes in heterogeneous media with diffuse waves. *Journal of the Acoustical Society of America*, *137*(2), 660–667. https://doi.org/10.1121/1.4906824

Pritchard, M. E., Allen, R. M., Becker, T. W., Behn, M. D., Brodsky, E. E., Bürgmann, R., et al. (2020). New opportunities to study earthquake precursors. *Seismological Research Letters*, *91*(5), 2444–2447. https://doi.org/10.1785/0220200089

Rouet-Leduc, B., Hulbert, C., Lubbers, N., Barros, K., Humphreys, C. J., & Johnson, P. A. (2017). Machine learning predicts laboratory earthquakes. *Geophysical Research Letters*, *44*(18), 9276–9282. https://doi.org/10.1002/2017GL074677

Rudnicki, J. W., & Chen, C. H. (1988). Stabilization of rapid frictional slip on a weakening fault by dilatant hardening. *Journal of Geophysical Research*, *93*(B5), 4745–4757. https://doi.org/10.1029/JB093iB05p04745

Shimazaki, K., & Nakata, T. (1980). Time-predictable recurrence model for large earthquakes. *Geophysical Research Letters*, *7*(4), 279–282. https://doi.org/10.1029/GL007i004p00279

Shreedharan, S., Bolton, D. C., Rivière, J., & Marone, C. (2020). Preseismic fault creep and elastic wave amplitude precursors scale with lab earthquake magnitude for the continuum of tectonic failure modes. *Geophysical Research Letters*, *47*(8), 1–10. https://doi.org/10.1029/2020GL086986

Shreedharan, S., Bolton, D. C., Rivière, J., & Marone, C. (2021a). Competition between preslip and deviatoric stress modulates precursors for laboratory earthquakes. *Earth and Planetary Science Letters*, *553*, 116623. https://doi.org/10.1016/j.epsl.2020.116623

Shreedharan, S., Bolton, D. C., Rivière, J., & Marone, C. (2021b). Machine learning predicts the timing and shear stress evolution of lab earthquakes using active seismic monitoring of fault zone processes. *Journal of Geophysical Research: Solid Earth*, *126*(7), 1–18. https://doi.org/10.1029/2020JB021588

Shreedharan, S., Rivière, J., Bhattacharya, P., & Marone, C. (2019). Frictional state evolution during normal stress perturbations probed with ultrasonic waves. *Journal of Geophysical Research: Solid Earth*, *124*(6), 5469–5491. https://doi.org/10.1029/2018JB016885

Snieder, R. (2002). Coda wave interferometry and the equilibration of energy in elastic media. *Physical Review E—Statistical Physics, Plasmas, Fluids, and Related Interdisciplinary Topics*, *66*(4), 8. https://doi.org/10.1103/PhysRevE.66.046615

Snieder, R. (2006). The theory of coda wave interferometry. *Pure and Applied Geophysics*, *163*(2–3), 455–473. https://doi.org/10.1007/s00024-005-0026-6

Snieder, R., Grêt, A., Douma, H., & Scales, J. (2002). Coda wave interferometry for estimating nonlinear behavior in seismic velocity. *Science*, *295*(5563), 2253–2255. https://doi.org/10.1126/science.1070015

Stähler, S. C., Sens-Schönfelder, C., & Niederleithinger, E. (2011). Monitoring stress changes in a concrete bridge with coda wave interferometry. *Journal of the Acoustical Society of America*, *129*(4), 1945–1952. https://doi.org/10.1121/1.3553226

Stanchits, S., Mayr, S., Shapiro, S., & Dresen, G. (2011). Fracturing of porous rock induced by fluid injection. *Tectonophysics*, *503*(1–2), 129–145. https://doi.org/10.1016/j.tecto.2010.09.022

van Uijlen, W. M. (2013). *Rotliegend geology in the Southern Permian Basin: The development of synrift sediments and its relation to seismic imaging*. Utrecht University. Retrieved from https://studenttheses.uu.nl/handle/20.500.12932/14228

Veltmeijer, A., Naderloo, M., & Barnhoorn, A. (2023a). Active and passive seismic monitoring of laboratory-based injection-driven fault reactivation. In *84th EAGE annual conference & exhibition* (pp. 1–5). European Association of Geoscientists & Engineers. https://doi.org/10.3997/2214-4609.202310513

Veltmeijer, A., Naderloo, M., & Barnhoorn, A. (2023b). Supporting data for the article "forecasting of rock failure in the laboratory using active acoustic monitoring methods [Dataset]. 4TU.ResearchData repository. https://doi.org/10.4121/21557910

Veltmeijer, A., Naderloo, M., Pluymakers, A., & Barnhoorn, A. (2022). Acoustic monitoring of laboratory induced fault reactivation. In *83rd EAGE annual conference & exhibition* (pp. 1–5). European Association of Geoscientists & Engineers. https://doi.org/10.3997/2214-4609.202210269

Wang, K., Johnson, C. W., Bennett, K. C., & Johnson, P. A. (2022). Predicting future laboratory fault friction through deep learning transformer models. *Geophysical Research Letters*, *49*(19), 1–9. https://doi.org/10.1029/2022GL098233

Wang, L., Kwiatek, G., Rybacki, E., Bonnelye, A., Bohnhoff, M., & Dresen, G. (2020). Laboratory study on fluid-induced fault slip behavior: The role of fluid pressurization rate. *Geophysical Research Letters*, *47*(6), 1–12. https://doi.org/10.1029/2019GL086627

Winkler, K., & Nur, A. (1979). Pore fluids and seismic attenuation in rocks. *Geophysical Research Letters*, *6*(1), 1–4. https://doi.org/10.1029/GL006i001p00001

Xie, F., Ren, Y., Zhou, Y., Larose, E., & Baillet, L. (2018). Monitoring local changes in granite rock under biaxial test: A spatiotemporal imaging application with diffuse waves. *Journal of Geophysical Research: Solid Earth*, *123*(3), 2214–2227. https://doi.org/10.1002/2017JB014940

Ye, Z., & Ghassemi, A. (2020). Heterogeneous fracture slip and aseismic-seismic transition in a triaxial injection test. *Geophysical Research Letters*, *47*(14), 1–9. https://doi.org/10.1029/2020GL087739

Zhang, Y., Abraham, O., Grondin, F., Loukili, A., Tournat, V., Duff, A. L., et al. (2012). Study of stress-induced velocity variation in concrete under direct tensile force and monitoring of the damage level by using thermally-compensated Coda Wave Interferometry. *Ultrasonics*, *52*(8), 1038–1045. https://doi.org/10.1016/j.ultras.2012.08.011

Zotz-Wilson, R., Boerrigter, T., & Barnhoorn, A. (2019). Coda-wave monitoring of continuously evolving material properties and the precursory detection of yielding. *Journal of the Acoustical Society of America*, *145*(2), 1060–1068. https://doi.org/10.1121/1.5091012

Zotz-wilson, R., Filippidou, N., Van Der Linden, A., Verberne, B. A., & Barnhoorn, A. (2020). Coda-wave based monitoring of pore-pressure depletion-driven compaction of Slochteren sandstone samples from the Groningen gas field. *Journal of Geophysical Research: Solid Earth*. https://doi.org/10.1002/essoar.10501522.2